

# Simultaneous ASCA and HST/GHRS observations of Cygnus X-2/V1341 Cygni

S. D. Vrtilek, J. C. Raymond

*Harvard-Smithsonian Center for Astrophysics, 60 Garden St., Cambridge MA 02138.*

*svrtilek@cfa.harvard.edu, jraymond@cfa.harvard.edu*

B. Boroson

*MIT, Cambridge, MA 02138. bboroson@space.mit.edu*

R. McCray

*JILA, University of Colorado, Boulder, CO 80309. DICK@jila.colorado.edu*

A. Smale, T. Kallman

*NASA/Goddard Space Flight Center, Greenbelt, MD 20177. alan@osiris.gsfc.nasa.gov,*

*tim@xstar.gsfc.nasa.gov*

F. Nagase

*ISAS, 3-1-1, Yoshimodai, Sagamihara, Kanagawa 229-8510. nagase@astro.isas.ac.jp*

## 1. Abstract

We present results from ultraviolet and X-ray observations of the low mass X-ray binary Cygnus X-2. The simultaneous HST/GHRS and ASCA observations took place during the low state of an 82-day cycle. We compare our observations as well as archival IUE and RXTE data with models that predict ultraviolet and optical continuum emission from an X-ray heated disk and a Roche-lobe-filling star. The model predictions are consistent with observed optical, ultraviolet, and X-ray variations over both orbital and long-term periods. The X-ray spectral state, the luminosities implied by fits to the X-ray data, the ultraviolet continuum and line fluxes, and the mass accretion rates obtained from fits to the ultraviolet continuum are consistent with location of our observations on the normal and horizontal branches of the Z-shaped X-ray color-color diagram. A combination of changes to mass accretion rate and obstruction by a warped disk can be invoked as a possible explanation for the motion of the “Z” in the color-color plane.

The GHRS/G160M measurements concentrated on NV ( $\lambda 1238.8$ ;  $\lambda 1242.8$ ) and HeII ( $\lambda 1640.5$ ). The low-resolution (GHRS/G140L) observations captured SiIV ( $\lambda 1393.8$ ;  $\lambda 1402.8$ ), NIV ( $\lambda 1486.5$ ), and CIV ( $\lambda 1548$ ); absorption lines detected in the spectra are interstellar. Although the relative line fluxes are consistent with emission from an X-ray heated accretion disk corona, predictions from models of line emission from simple disks do not fit the observed emission line profiles. The lack of double peaks suggests that most of the line emission is from the surface of the companion and the radial velocities (80-130 km s<sup>-1</sup>) are consistent with emission from the optical star at the orbital phase (0.70-0.74) of our observations.

stars: neutron – X-rays: binaries –X-rays: individual (Cygnus X-2)

## 2. Introduction

Cygnus X-2 <sup>1</sup> is a low mass X-ray binary (LMXB) with an orbital period of 9.843 days (Cowley, Crampton, & Hutchings 1979). Its optical companion, V1341 Cygni, is a  $0.7M_{\odot}$  star of 15th magnitude with spectral type varying from A5 to F2. RXTE observations have shown the presence of a long-term period between 78-82 days in Cyg X-2 which has since been confirmed with data from earlier missions (Wijnands, Kuulkers, & Smale 1996; Paul, Kitamoto, & Makino 2000).

Cyg X-2 is a “Z-source”: an LMXB which shows three distinct X-ray spectral states, referred to as the flaring, normal, and horizontal branches (FB, NB, and HB), which form a ‘Z’ shape on an X-ray color-color diagram. While Cyg X-2 displays no high-Q pulsations, each state shows distinct modes of quasi-periodic oscillations (QPOs) in X-ray emission. Cyg X-2 is the only “Z-class source” that regularly displays all three X-ray spectral states (FB, NB, and HB) with their associated QPOs and is bright in the ultraviolet (Hasinger *et al.* 1990; Vrtillek *et al.* 1990 [hereafter Paper I]). It is also among the Z-sources that show significant motion of the Z pattern on the color-color plane (Wijnands *et al.* 1997).

Simultaneous ultraviolet and X-ray observations of LMXBs show a unique relationship between the X-ray spectral states and the ultraviolet flux. Sco X-1 and Cyg X-2, the two brightest Z-sources, have ultraviolet flux that is directly correlated with the X-ray spectral state of the source (Paper I; Vrtillek *et al.* 1991a); there is a factor-of-three increase in ultraviolet flux from the HB to the FB. Most of the optical and ultraviolet luminosity ( $L_{opt} \sim L_{ultraviolet} \sim 10^{-2}L_X$ ) likely comes from the accretion flow as it is illuminated by the X-rays from the neutron star. The ultraviolet spectra of Cyg X-2 and Sco X-1 (Paper I; Vrtillek *et al.* 1991a) are dominated by strong emission lines of N V  $\lambda$  1240, C IV  $\lambda$  1550, and He II  $\lambda$  1640. The ultraviolet line strengths, ratios, and profiles vary noticeably ( $\sim 20\%$ ) on the shortest timescales ( $\sim 30$ min for Sco X-1 and  $\sim 120$ min for Cyg X-2) that can be

---

<sup>1</sup>Based partially on observations with the NASA/ESA Hubble Space Telescope, obtained at the Space Telescope Science Institute, which is operated by the Association of Universities for Research in Astronomy, Inc. under NASA contract No. NAS5-26555.

probed with IUE. There is evidence that the X-ray lines in Cyg X-2 vary in the same way as the ultraviolet lines in that both are enhanced during the FB (Vrtilek *et al.* 1991a,b).

Here we present simultaneous ultraviolet and X-ray observations of Cyg X-2 taken with the GHRS on HST and the GIS and SIS detectors on ASCA. With HST we can for the first time measure variability of the ultraviolet spectra of LMXBs on short ( $50 \text{ ms} \leq \Delta t \leq 30 \text{ min}$ ) timescales. This enables a search for an ultraviolet manifestation of the QPOs observed in X-rays. Finding QPOs in the ultraviolet would be important: whereas the X-ray flux can be easily modulated by geometric effects and emission in the visible can be confused with that of the non-collapsed secondary, the ultraviolet observations are most likely to yield direct evidence of phenomena related to the accretion disk. In addition the HST spectral resolution,  $\Delta V \sim 19 \text{ km s}^{-1}$  (HRS G160M), enables the dissection of accretion flows according to velocity, a measurement of local physical conditions and dynamics that the X-ray observations cannot do. From delays between X-ray and ultraviolet line variations, the radial structure of velocity in the disk can be analyzed. This provides an unprecedented probe into the structure and dynamics of the accretion flow, enabling us to test models of the ultraviolet emission and constrain properties of the secondary star.

In this paper we compare the simultaneous HST/GHRS and ASCA data as well as archival IUE data with models predicting ultraviolet continuum emission from the X-ray heated disk and star. We interpret the double-peaked long-term period of Cyg X-2 in terms of a saddle shaped disk. The ultraviolet spectral features are tested with simple models for line emission from a disk and from an X-ray heated corona above the disk. A comparison is made of the ultraviolet spectra of Cyg X-2 with those of similar binary systems taken with the GHRS. The observations and analysis are presented in section 3 and our interpretation is discussed in section 4.

### 3. Observations and Analysis

Figure 1 shows the location of our observation in comparison with the one-day averaged lightcurves obtained from the All Sky Monitor (ASM) on RXTE provided by the

RXTE/ASM team. A description of the RXTE can be found in Levine *et al.* (1996). Since the ASM data currently available cover a considerably longer time than those used by Wijmands, Kuulkers, & Smale (1996) we re-determined the long-term period using an Analysis of Variance (ANOVA) method with (F-statistic) as described in Davies (1990;1991). For the data shown in Figure 1 our most significant period is  $82.5 \pm 2.5$  days; using the entire RXTE data set to date (through April 2003) we find  $81.7 \pm 0.6$  days; we use the 81.7 day period in this paper. The 82-day cycle has two maxima and two minima; we define phase zero as the center of the deepest minimum. Figure 1c shows the 82-day lightcurve we determine and Figure 1b the lightcurve superposed on the data. This indicates that our simultaneous HST and ASCA observations occurred during one of the low states of the 82-day cycle.

The ASCA lightcurves and HST coverage are plotted in Figure 2. The HST/GHRS took eight separate observations on 1995 Dec. 7 from 3:26 UT (JD 2,450,058.643) to 1995 Dec. 7 12:49 UT (JD 2,450,059.034) which covers the orbital phases 0.70-0.74. ASCA observed Cyg X-2 from 1995 Dec. 6 22:15 UT (JD 2,450,058.427) to 1995 Dec. 7 22:01 UT (JD 2,450,059.417) covering the orbital phase range 0.68-0.78. The orbital phases were calculated using an ephemeris of JD2443161.68 for phase 0.0 and a period of 9.843 d (Cowley, Crampton, & Hutchings 1979), where phase 0.0 refers to superior conjunction of the optical star.

The first four HST observations were taken with the GHRS G160M ( $17 \text{ km s}^{-1}$ ) grating centered alternately on  $1240\text{\AA}$  (N V) and  $1640\text{\AA}$  (He II) in the RAPID mode with a time resolution of 0.5s (Figure 3). A description of the GHRS and gratings is given by Cardelli, Savage, & Ebbets (1990). The GHRS observations were taken after the installation of COSTAR and the repairs to the faulty electronics of side 1. The last four observations used the GHRS/G140L ( $140 \text{ km s}^{-1}$ ) in the wavelength region  $1220\text{--}1550\text{\AA}$  in order to test for ultraviolet continuum and line strength variability (Figure 4). The G140L was used in RAPID mode with a time resolution of 50ms to search for the quasi-periodic oscillations so far seen only in the X-rays. Our use of the GHRS in the RAPID mode prevented us from over-sampling the spectrum, checking for bad counts, and correcting for the Doppler

shift due to the spacecraft orbit. In addition, the continua for the G160M exposures are poorly determined because most of the counts ( $\sim 80\%$ ) are due to background. Hence the standard products produced for counts per diode per time interval are not suited for temporal variability studies.

The X-ray countrates from both the GIS and SIS detectors on ASCA (described in Tanaka, Inoue, & Holt [1994]) varied by less than 10% during our observation. Consequently the X-ray color-color diagram covers only a small segment of the ‘Z’ (Figure 5). The slope, when compared to the complete Z shown by Hasinger *et al.* (1990), suggests that we are on the HB, possibly at the turning point into the NB. No significant dips in X-ray countrate were visible during our observation.

Much of our SIS data were taken in FAST mode which presents problems for spectral analysis. FAST mode complicates the removal of flickering pixels. Also, the response depends on position and there is no position information in FAST mode. We obtained the FAST mode data for the timing analysis (search for QPOs). Our SIS BRIGHT mode data of Cyg X-2 suffer from pile-up because the count rate is so high. Pileup arises when more than one photon is collected in the same pixel (or neighboring pixels) in the SIS CCDs within an integration time (4 seconds for BRIGHT mode.) The result of pileup is that multiple input photons are not detected separately, but a signal is recorded corresponding to the sum of the energies of the photons. Thus pileup can falsely increase the high-energy part of the spectrum while decreasing the low-energy spectrum. (The latter effect is usually negligible, as the counts peak at low energies.)

Our treatment of pileup follows that of Ebisawa *et al.* (1996). For analysis of the SIS BRIGHT mode spectra, we discard the central circle of 13 pixel radius, as this is the region in which pileup is most severe. Then we construct a model of the high energy spectrum produced by piled-up photons using Ebisawa’s algorithm; this model is subtracted from the total counts before fitting. Piled-up counts contribute 10% at 5 keV and 30% at 8 keV, according to Ebisawa’s analysis. With the central 13 pixel radius region removed, the count rate is  $86 \text{ cts s}^{-1}$  with a piled up rate of  $1.5 \text{ cts s}^{-1}$  for A1-3 (A4 had no BRIGHT mode

data); without the central region removed the count rate is  $140 \text{ cts s}^{-1}$  and the piled up count rate is  $4.6 \text{ cts s}^{-1}$ . Once the model for the pileup is taken into account, the SIS BRIGHT mode spectra agree with the GIS models (detailed below) for  $E > 1 \text{ keV}$ . Below  $1 \text{ keV}$  pileup effects are too strong to correct.

### 3.1. Continuum Fits

We used basic parameters for the source as found in Cowley, Crampton, and Hutchings (1979), McClintock *et al.* (1984) and paper I: a distance to the source of 8 Kpc; an  $E_{B-V}$  of 0.45; and a  $0.7 M_{\odot}$  F star companion with an effective temperature of 7,000K. We assume that the 82-day period is due to a warping and precession of the disk induced by the effects of uneven X-ray irradiation on the disk. This is a commonly accepted means for producing superorbital periods in systems such as Her X-1, LMC X-4, and SMC X-1 (Clarkson *et al.* 2002; 2003; Cheng, Vrtilek, & Raymond 1995; Vrtilek *et al.* 1997).

#### 3.1.1. Ultraviolet: HST and IUE

##### *Disk Model*

We simulate the warp with a saddle-shape for the inner disk of Cyg X-2 (Figure 6), in order to reproduce the double-peaked shape of the long-term X-ray lightcurves. In effect the shape of the disk is an “inversion” of the average X-ray lightcurve. To determine the inversion, we loop through 28,800 points (120 points in latitude and 240 points in longitude) on the neutron star surface. This corresponds to a grid coarseness of  $0.025 r_{NS}$ ; refining the grid by a factor of two in each dimension gives the same result within errors, so this number of grid points should be sufficient. For each point, the program computes analytically whether the line towards the viewer intersects the disk. We follow Howarth & Wilson (1983a,b) in that the coordinates are fixed to the disk so that it is the line-of-sight that changes with the long-term phase. This coordinate system allows us to specify the shape of the disk in a frame in which it does not vary over the long-term phase. The

equation of the saddle-shaped disk is given by  $z_d = \pi\theta_w(y_d^2 - x_d^2)/180r_d$  for ( $r_d < 1.7r_{NS}$ ); it is constrained to revert to a simple disk ( $z_d = 0$ ) in the orbital plane for large radii ( $r_d \geq 1.7r_{NS}$ ).

The parameters describing the disk, listed in Table 1, are the radius of maximum disk warp,  $R_{mw}$ ; the disk thickness,  $\theta_d$ , in degrees; the tilt of the disk from the orbital plane,  $\alpha_d$ ; and the line-of-nodes parameter,  $\Delta\psi$  (this parameter is “invisible” in the sense that it does not count against the  $\chi^2$  but sets the phase origin of the model relative to the observed long-term X-ray light curve). Our best-fit parameters are a maximum saddle height of  $1.3r_{NS}$  at a distance of  $1.7r_{NS}$  radius with a tilt of the inner disk from the orbital plane of  $\alpha_d=4.1\pm0.4$  degrees at long-term phase 0.5 (Table 1). The tilt of the inner disk from the orbital plane allows for the uneven depths of the lightcurve: at long-term phase 0.0 the disk is tilted away from the observer causing a deeper dip than at long-term phase 0.5. The X-ray flux we see, as determined by the amount of X-rays that are hidden by the saddle-shaped inner disk, is compared to the RXTE ASM data in Figure 7. This is also the flux seen by the outer disk and the companion star.

### *X-ray reprocessing*

We adapt our model for determining continuum flux from X-ray reprocessing on the companion star and disk as described in Paper I in several ways: (1) We replace the spherical shape assumed for the companion star in Paper I with a tidally distorted shape that represents the filled Roche lobe of V1341 Cygni as was done for Her X-1 by Cheng, Vrtillek, & Raymond (1995). (2) Instead of computing the temperature due to X-ray heating on each of 40 points on the companion star surface we computed the temperature at 7200 points (120 in longitude and 60 in latitude). (3) The disk is represented in 3-dimensions by using 1000 annular rings divided into viewing angles determined by a 15 by 29 array for each of 8 “quadrants”.

Given the shape of the disk and a distorted Roche-lobe filling companion star we calculate the flux over the range 1150-7427Å. At each point on the companion star and



the disk a temperature due to X-ray heating is computed; the contribution to the flux is determined by summing spectra from the library of observed stellar spectra (Cannizzo & Kenyon 1987) for a star at the computed temperature.

Predictions of the model from the ultraviolet and optical U and V bands are shown in Figure 8. The U and V optical predictions are compared to published photometry of Cowley, Crampton, and Hutchings (1979) and Chevalier, Bonazzola, and Ilovaisky (1976). The extremes of U and V magnitudes reported are given as dotted lines in Figure 8. We have used archival IUE data for comparison with the ultraviolet predictions. Since the GHRS had a limited continuum coverage (Fig. 4) we integrated over the wavelength regions 1340-1380Å and 1420-1480Å to compare the UV fluxes. For the optical V band we integrated over the range 5000-6000 Å and for the U band over 3510-3520Å (although the U band is centered on 3500Å the stellar library [Cannizzo & Kenyon 1987] that we use to determine fluxes has no values between 3200-3500Å). We then converted the computed fluxes to magnitudes using formulae taken from Lang (1980).

Because the 82-day period has a large uncertainty the long term phase of the optical and IUE observations cannot be determined. The predicted U magnitudes fully encompass the range observed; the predicted V magnitudes overlap with, but are on average greater than, the reported extremes. The ultraviolet data—including the current observations and all archival IUE observations—fall within extremes given by a lower limit to  $\dot{M}$  of  $3.2 \times 10^{-9} M_{\odot} \text{ yr}^{-1}$  and an upper limit of  $1.8 \times 10^{-8} M_{\odot} \text{ yr}^{-1}$ , consistent with the results of Paper I. There is uncertainty in the flux level, both for the model and the data. The HST data are calibrated to only 10% in absolute flux, and there is a difference in resolution between IUE and GHRS. As for the model, uncertainties in reddening and stellar temperature can shift the flux (see the Appendix in Paper I for a discussion of these uncertainties). The relative errors in flux are likely to be much smaller than the uncertainty in overall flux normalization. The best fit to the HST continuum data (shown as a filled triangle) corresponds to an  $\dot{M}$  of  $6.0 \times 10^{-9} M_{\odot} \text{ yr}^{-1}$ ; this is consistent with a location in the HB (Paper I) (Figure 4; the thin solid lines represent the models). The  $\dot{M}$  values computed by applying this model to the G160M data (observations H2 and H3; Figure 3) were somewhat

higher. Either we caught the source at the upper bend of the ‘Z’ where the HB connects with the NB or the very small continuum band available in the G160M is not sufficient to constrain the model properly and the  $\dot{M}$  values are not reliable (here the background is much greater than the continuum).

### 3.1.2. X-ray: ASCA

The X-ray spectra observed with the ASCA GIS were modelled with the sum of Comptonized bremsstrahlung (following Sunyaev & Titarchuk 1980), a blackbody, and an emission line at  $\approx 1$  keV (Table 2). In Figure 9 we show the spectra from the ASCA observations divided into three intervals: A1-A4; A6-18; and A9-A11; an observation of Cyg X-2 taken during ASCA’s performance verification phase is also depicted (Smale *et al.* 1994). The region around 2.2 keV is excluded due to an instrumental effect not fully accounted for in the calibration (Mukai, personal communication 1996). The spectral fits are consistent with interval A6-A8 located on the upper NB, the PV phase observation on the HB, and intervals A1-A4 and A9-A11 in a transition from the HB to the NB. Specifically the blackbody component is reduced in the HB and line emission is enhanced in the NB; we note that a blackbody component is present in Cyg X-2 at all phases of the Z with the *exception* of the upper HB (Kuulkers, van der Klis, & van Paradijs 1995). The luminosities implied by the above spectral fits for an assumed distance of 8 kpc ranges from  $(3-5) \times 10^{37}$  ergs s $^{-1}$  consistent with the HB and the upper NB as inferred by the ultraviolet continuum fits. The reality of the emission features around 1 keV have been questioned by Psaltis, Lamb, & Miller (1995; PLM95) who are able to fit ASCA data of Cygnus X-2 with a Comptonized thermal emission model that does not require spectral features. They suggest that features near 1 keV may be due to known problems in Comptonization models. An approximation to the PLM95 model assumes that below a given energy (taken as a free parameter) the spectrum is a blackbody, while above that energy it has a Comptonized shape, with temperature equal to that of the blackbody. We find that fits of these models are not as good as the Comptonized + blackbody + line models; e.g.,  $\chi^2_{\nu}=1.42$  instead of 0.995 for A1-A4

and  $\chi^2_\nu=1.73$  instead of 1.22 for A9-11. The transition energy between the blackbody and Comptonized components occurs at a low energy ( 0.6 keV). Line features around 1 keV have been reported for Cyg X-2 by several observers: Vrtilek *et al.* 1986, 1988 reported lines in Einstein OGS and SSS spectra of Cyg X-2, attributing a line at 0.96 keV with Fe XX and Ni XX and a line at 1.12 keV with Fe XXIII-XXIV. The presence of these features was confirmed by Kuulkers *et al.* (1997) using the Low Energy Concentrator Spectrometer on-board *BeppoSAX*. In addition, Branduardi-Raymont *et al.* (1984) using *Ariel V* Experiment C, Chiappetti *et al.* (1990) using the EXOSAT CMA, Lum *et al.* (1992) using the *Einstein* Focal Plane Crystal Spectrometer, and Smale *et al.* (1993; 1994) using the Broad Band X-ray Telescope and the ASCA SIS all report evidence for excess emission near 1 keV from Cyg X-2 (cf. Kuulkers *et al.* 1997).

### 3.2. Ultraviolet Spectral Features

Table 3 gives the line fluxes and velocities for the G160M and G140L observations shown in Figures 3 and 4. The velocities are determined from flux-weighted wavelengths and are consistent with those observed in optical (He II 4686) by Cowley, Crampton, & Hutchings (1979) for the orbital phase of our observations (0.70-0.74). The error in the fluxes include both counting statistics and uncertainties introduced by choosing background and wavelength boundaries. No significant change is observed during the different observations, which is not surprising since they cover a very small fraction of the binary phase space. The N V doublet is clearly resolved with the doublet ratio close to 1.2:1 rather than the 2:1 expected from thin accretion disks. A similar result was found from GHRS observations of Sco X-1 (A N V doublet ratio of 1.1:1; Kallman, Boroson, & Vrtilek 1998) and the narrow lines seen in Her X-1 (ratio 1.2:1; Boroson *et al.* 1996). The Cyg X-2 N V lines can also be fit by including a broad emission component (Figure 10) such as was observed in Her X-1; but this is not required. For the C IV line we were only able to get an upper limit to the line flux, as the line is cut off by the edge of the detector. For this line, the line velocity is found by flux-weighting the wavelengths only near the peak, not over the

entire line profile (where the flux is greater than the background) as for the other lines.

In Figure 11 we show a composite of the four GHRs G140L spectra of Cyg X-2 together with those of Sco X-1 (Kallman, Boroson, & Vrtilek 1998) and Her X-1 (Boroson *et al.* 1997). In each case the solid line depicts the best-fit X-ray heated accretion disk model for the continuum. (The slope in the Her X-1 continuum spectrum is due to the strong contribution from the star; for Cyg X-2 and Sco X-1 the continuum is dominated by X-ray heating of the disk). While the saddle-shaped disk provides good fits to the continuum emission, the intensities of many of the spectral features remain unaccounted for by photoionization models, such as the XSTAR code (Kallman & McCray 1982; Kallman & Krolik 1993). For both Sco X-1 and Her X-1 the O V line at 1371 Å is surprisingly strong compared to N V, contrary to theoretical expectations (Raymond 1993, Ko & Kallman 1994), whereas Cyg X-2 showed no O V  $\lambda$ 1371 and relatively strong N IV  $\lambda$ 1486. Since Sco X-1 and Cyg X-2 are both LMXBs of the same type the differences in their ultraviolet spectra and the similarity of the Sco X-1 and Her X-1 ultraviolet spectra is surprising. The N V line in Her X-1 (not shown) is much stronger than the C IV line suggesting abundance anomalies (Raymond 1993). Cyg X-2 and Her X-1 have similar mass accretion rates when Cyg X-2 is in the HB. The difference in flux can be attributed to reddening and distance effects. The presence of N IV], its strength relative to other lines, and the absence of O V in Cyg X-2 are consistent with the predictions of Raymond (1993) model F. Since N IV] is an intercombination line which requires somewhat lower densities it is produced preferentially at the outer edges of the disk where densities are lower. Cyg X-2 has a larger disk (outer disk radius =  $3 \times 10^{11}$  cm [Paper I]) than either Her X-1 (outer disk radius =  $\sim 10^{11}$  cm [Cheng, Vrtilek, & Raymond 1995]) or Sco X-1 (outer disk radius =  $3 \times 10^{10}$  cm [Vrtilek *et al.* 1991a]). Of the 10 models listed by Raymond (1993) none show O V that do not *also* show N IV] at a comparable or greater strength. Raymond extrapolates from his models that the density will be about  $\sim 3 \times 10^{13}$  cm $^{-3}$  at a radius of  $3 \times 10^{11}$  cm; the lower density estimates of Paper I probably result from the assumption that the N V emission line is effectively optically thin. Kallman, Boroson, & Vrtilek (1998) point out that the O IV  $\lambda$ 1340 and O V  $\lambda$ 1370 lines are subordinate lines, and so require either that the emitting ions be in

an excited state, or that excitation occur from the ground state through a dipole-forbidden transition. The former case requires a combination of high gas density and optical depth in the resonance line leading to the level from which excitation can occur. This can be expressed as  $n\tau \geq 10^{16} \text{ cm}^{-3}$ . Such densities and optical depths are predicted to occur in X-ray heated disk atmospheres (Ko and Kallman 1994).

#### 4. Discussion and Conclusions

As first demonstrated in Paper I, X-ray heating of a disk and companion star provide good fits to the continuum ultraviolet emission from Cyg X-2/V1341 Cyg. We have refined the model described in Paper I by using a distorted Roche-lobe filling surface for the optical companion. Owing to the low temperature of the companion star the contribution from the unheated star to the ultraviolet flux is minor: the primary contribution to the UV continuum is X-ray heating effects on the disk. We further changed the model in Paper I by distorting the inner edge of the accretion into a saddle-shape that reproduces the average X-ray lightcurve. The reason for changing only the inner disk are twofold: the distortion is due to X-ray heating effects and these are maximum in the inner disk; the disk in Cyg X-2 is rather large ( $3 \times 10^{11} \text{ cm}$ ) and even small changes in the outer disk would completely obscure the central X-ray emission. van Kerkwijk *et al.* (1998) define a parameter  $F^*$  that describes where in a disk warping occurs. When  $0.1 < F^* < 0.15$ , the outer disk is warped, when  $0.15 < F^* < 0.2$ , the inner disk can be warped also, and when  $F^* > 0.2$ , the inner disk can be tilted by  $> 90$  degrees and may behave chaotically.  $F^*$  depends on the albedo of the disk and the albedo can change as a function of angle of incidence: if we could prove that only warping of the inner disk provides a solution than we have a limit on  $F^*$  and from that a limit on albedo. We have not yet found a way to make the model work by warping only the outer disk

The  $\dot{M}$  values necessary to fit the simultaneous GHRS/ASCA data we analyze here are well within the range obtained using simultaneous IUE/EXOSAT data of the system (Paper I). We have increased these limits here in order to enclose ALL IUE observations

of the system. While the highest flux predicted by the model in the V band is greater than the highest V magnitudes reported, the range in magnitude has the same excursion as that observed. The UV flux and U magnitude measurements lie well within the model predictions.

The line profiles of He II and N V obtained with the G160M grating do not show the double-peaked structure that is predicted by simple models of line emission from disks. This suggests that most of the line emission observed is from the surface of the companion; the measured line velocities are consistent with this picture; however, the FWHMs are larger than expected. It is also possible that the line emission is from an accretion heated corona above the disk: the relative strengths of the features observed for Cygnus X-2 are consistent with the predictions of Raymond (1993); however, the FWHMs are then smaller than expected.

The relatively low-resolution GHRS observations are not able to separate many line components that STIS will be able to resolve. For example, if N IV] is preferentially produced at the outer region of the disk and the line widths are due primarily to Keplerian velocities, we would expect it to be narrower than the other lines (the outer disk rotates more slowly), that can also be formed in the inner disk. While there is some variation over the four G140L observations, the average values support this conclusion, with N IV] having an average FWHM of  $398 \text{ km s}^{-1}$  whereas Si IV  $\lambda 1393$  averages to  $600 \text{ km s}^{-1}$  and Si IV  $\lambda 1402$  averages to  $459 \text{ km s}^{-1}$  (this is a  $\sim 1\sigma$  determination given our velocity resolution of  $140 \text{ km s}^{-1}$ ).

The HST/STIS HST, extends in several significant ways the ultraviolet capabilities that were available with the GHRS: with the echelle grating it is possible to sample continuously a broad region ( $600\text{\AA}$ ) of the spectrum at greater spectral resolution than with the GHRS. STIS offers another improvement over the GHRS: a lower background (the STIS dark count rate is  $7.0 \times 10^{-6} \text{ counts s}^{-1} \text{ pixel}^{-1}$  which is 50-100 times lower than that of the GHRS). For the GHRS, the background was not negligible compared with the source flux; in order of increasing severity, this hampered the line, continuum, and variability

studies. STIS observations will allow us to refine these as well as to investigate the physical condition of the emitting gas through line and doublet ratios.

The X-ray spectra are well fit with the sum of a Comptonized bremsstrahlung, a blackbody, and an emission complex around 1 keV. We note that if we associate the Comptonized component with the neutron star and the blackbody+lines with emission from the disk then the motion of the Z shape in the color-color diagram could be attributed to the varying amounts of each component that are covered by the disk. This can be tested by looking at the source during the high and the low states of the cycle: the motion of the Z should be correlated with the long-term period. The correlation will not be absolute since the X-ray components also vary in strength depending on mass accretion rate.

SDV was supported by NASA through Grants NAG5-6711, and GO-07288.01-96A from the Space Telescope Science Institute, which is operated by AURA, Inc., under NASA contract NAS5-26555.

## References

- Boroson, B., Vrtillek, S.D., McCray, R., Kallman, T.R., & Nagase, F. 1996, ApJ, 473, 1079.
- Boroson, B., Blair, W. P., Davidsen, A. F., Vrtillek, S.D., Raymond, J.C., Long, K. S., & McCray, R. 1997, ApJ, 491, 903.
- Branduardi-Raymont, G., Chiapetti, L., Ercan, E.N., 1984, A&A, 130, 175.
- Canizzo, J.K., & Kenyon, S.J. 1987, ApJ, 320, 319
- Cardelli, J. A., Savage, B. D., & Ebbets, D. G. 1990, ApJ, 365, 789.
- Cheng, F.H., Vrtillek, S.D., & Raymond, J.C. 1995, ApJ, 452, 825
- Chevalier, C., Bonazzola, S., & Ilovaisky, S.A. 1976, A&A, 53, 313.
- Chiapetti, L., Treves, A., Branduardi-Raymont, G. *et al.* 1990, ApJ, 361, 596.
- Clarkson, W.I., Charles, P.A., Coe, M.J., Laycock, S., Tout, M.D., & Wilson, C.A. 2003, MNRAS, 339, 447
- Clarkson, W.I., Charles, P.A., Coe, M.J., & Laycock, S. 2003, MNRAS, in press, astro-ph 0304073.
- Cowley, A.P., Crampton, D., & Hutchings, J.B. 1979, ApJ, 231, 539.
- Davies, S.R. 1990, MNRAS, 244, 93
- Davies, S.R. 1991, MNRAS, 251, 64
- Ebisawa, K., Ueda, Y., Inoue, H., Tanaka, Y., & White, N. E. 1996, ApJ, 467, 419.
- Hasinger, G., van der Klis, M., Ebisawa, K. Dotani, T., Mitsuda, K. 1990, A&A, 235, 131.
- Howarth, I.D., & Wilson, B. 1983a, MNRAS, 204, 347.
- Howarth, I.D., & Wilson, B. 1983b, MNRAS, 204, 1091.
- Kallman, T.R., Boroson, B., & Vrtillek, S.D. 1998, ApJ, 502, 441.



- Kallman, T.R., & Krolik, J. 1993, NASA Internal Report.
- Kallman, T.R., & McCray, R. 1982, ApJS, 50, 263.
- Ko, Y.K., & Kallman, T.R. 1994, ApJ, 431, 273.
- Kuulkers, E., Parmar, A.N., Owens, A., Oosterbroek, T., & Lammers, U. 1997, A&A, 323, L29.
- Kuulkers, E., van der Klis, M., Van Paradijs, J., 1995, ApJ, 450, 748.
- Lang, K.R. 1980, Astrophysical Formulae, Springer-Verlag: New York.
- Levine, A.M., *et al.* 1996, ApJ, 469, L33.
- Lum, K.L., Canizares, C.R., Clark, G.W., *et al.* 1992, ApJ, 78, 423.
- McClintock, J.E., Petro, L.D., Hammerschlag-Hensberge, G., Proffitt, C.R., & Remillard, R.A. 1984, ApJ, 283, 794
- Morrison, R., & McCammon, D. 1983, ApJ, 270, 119.
- Paul, B., Kitamoto, S., & Makino, F. 2000, ApJ, 528, 410
- Psaltis, D., Lamb, F.K., and Miller, G. 1995, ApJ, 454, L137
- Raymond, J.C. 1993, ApJ, 412, 267.
- Smale, A. P., Angelini, L., White, N. E., Mitsuda, K., & Dotani, T. 1994, BAAS, 185, 102.
- Smale, A.P., Done, C., Mushotzky, R.F., *et al.* 1993, ApJ, 410, 796.
- Sunyaev, R.A. & Titarchuk, L.G. 1980, A&A, 86, 121.
- Tanaka, Y., Inoue, H., & Holt, S.S. 1994, PASJ, 46, L37.
- van Kerkwijk, M.H., Chakrabarty, D., Pringle, J.E., & Wijers, R.A.M.J. 1998, ApJ, 499, L27.
- Vrtilek, S.D., Boroson, B., Cheng, F.H., McCray, R., & Nagase, F. 1997, ApJ, 490, 377.

Vrtilek, S.D., Kahn, S.M., Grindlay, J.E., Helfand, D.J., & Seward, F.D. 1986, ApJ, 307, 698.

Vrtilek, S.D., McClintock, J.E., Seward, F.D., Kahn, S.M., & Wargelin, B.J. 1991a, ApJS, 76, 1127.

Vrtilek, S.D., Penninx, W., Raymond, J.C., Verbunt, F., Hertz, P., Wood, K., Lewin, W.H.G., & Mitsuda, K. 1991b, ApJ, 376, 278.

Vrtilek, S.D., Raymond, J.C., Garcia, M.R., Verbunt, F., Hasinger, G., & Kurster, M. 1990, A&A 235, 162 (Paper I).

Vrtilek, S.D., Swank, J.H., Kallman, T.R. 1988, ApJ, 326, 186.

Wijnands, R.A.D., Kuulkers, E., & Smale, A.P. 1996, ApJ, 473, L45.

Wijnands, R.A.D., van der Klis, M., Kuulkers, E., & Hasinger, G. 1997, A&A, 323, 399.

## Figure Captions

**Figure 1.** (a) One day averages of the flux observed from Cyg X-2 with the All Sky Monitor on board the ROSSI X-ray Timing Explorer. (Quick-look results were provided by the ASM/RXTE team.) (b) The data from (a) (histograms) with the lightcurve from (c) (smooth curve) superposed. (c) The lightcurve obtained by folding all RXTE/ASM data with a period of 81.7 days). In (c) the arrow indicates the time of the simultaneous HST/ASCA observations.

**Figure 2.** X-ray lightcurves (0.6-10 keV) from 1995 Dec. 6 22:15 UT to 1995 Dec. 7 22:01 UT (from SIS1 on ASCA) and ultraviolet coverage (with GHRS on HST). The numbers A1-A11 refer to ASCA orbit. The numbers H1-H8 refer to HST observation. The GHRS filters and wavelength ranges are indicated.

**Figure 3.** HST/GHRS G160M observations. H1 and H2 are centered on N V. H3 and H4 are centered on HeII. The thin solid lines show the best fit to the continuum using the model described in Section 3.

**Figure 4.** HST/GHRS G140L observations. The thin solid lines show the best fit to the continuum using the model described in Section 3.

**Figure 5.** An X-ray color-color diagram for the ASCA data. The ratio taken is that of photon counts uncorrected for effective area. A schematic “Z-curve” is drawn on for comparison.

**Figure 6.** The saddle-shape used for the the inner edge of the disk. Lines-of-sight to the observer at long-term phases of X-ray maxima (0.25 and 0.75) and X-ray minima (0.5 and 0.0) are indicated.

**Figure 7.** Histograms represent the RXTE ASM data. The X-ray flux predicted from the saddle-shaped disk is depicted as a dotted line. The dashed line is a sinusoidal fit (fundamental plus 1st harmonic):  $a \sin (2\pi(t-t_o)/82\text{days}) + b(2\pi(t-t_o)/41 \text{ days})$ . Fits of

the saddle model to the data give a  $\chi^2_\nu$  of 1.8 whereas the fit using 2 sinusoids gives a  $\chi^2_\nu$  of 3.2. per degree of freedom.

**Figure 8.** In all three panels the dotted lines represent X-ray low-states and dot-dashed lines represent X-ray high states of the 82-day period. The upper curves are computed for the highest  $\dot{M}$  and the lower curves the lowest  $\dot{M}$  required to include the observed UV fluxes. (a) Shows average UV continuum flux predicted by the model near N V vs. binary phase. The solid triangle represents the GHRS observations and the open triangles are archival IUE data. (b) The V magnitude predictions of the model (average over 5000-6000Å). The dashed lines denote the extremes of V observed for the system. (c) The U magnitude predictions of the model (average over 3510-3520Å; The IUE flux library used for our model have no values between 3200-3500Å). The dotted lines represent extremes of U magnitudes reported for Cyg X-2.

**Figure 9.** Histograms represent data shown as unfolded photon spectra. Typical error bars are depicted in each panel. (a) ASCA GIS 3 spectrum for orbits A1-A4. (b) ASCA GIS 3 spectrum for orbits A6-A8. (c) ASCA GIS 3 spectrum for orbits A9-A11. (d) ASCA GIS 3 spectrum for the PV phase observation. The solid lines represent the best-fit models as listed in Table 2. The dotted lines show the Comptonized Bremsstrahlung component; the long dashes the blackbody component; and the short dashes the line complex near 1 keV.

**Figure 10.** An HST G160M observation of the N V doublet. The narrow lines have velocities of -93 and -94 km s<sup>-1</sup> with FWHMs of 316 and 336 km s<sup>-1</sup>. The broad lines (not listed in Table 3) have velocities of -210 km s<sup>-1</sup> with FWHM of 1000 km s<sup>-1</sup>.

**Figure 11.** A comparison of HST GHRS 140L observations of Cyg X-2, Sco X-1, and Her X-1. The solid lines show the best-fit to the continuum using X-ray heated disk and companion star. The corresponding mass-accretion rates are noted.

TABLE 1. PARAMETERS USED FOR ULTRAVIOLET CONTINUUM FITS<sup>1</sup>

Parameter	Value
Mass of neutron star $M$	$1.4M_{\odot}$
Mass ratio $q = (M_{NS}/M_{star})$	2.0
Temperature of normal star	7000K
E(B-V)	0.45
Distance to source	8.0 kpc
Separation $a$	$1.8 \times 10^{12} \text{cm}$
Inner disk radius $r_1$	$1.0 \times 10^6 \text{cm}$
Outer disk radius $r_2$	$3.0 \times 10^{11} \text{cm}$
Gravity darkening exponent $\beta$	0.08
Limb darkening coefficient	0.8
Inclination angle of orbital plane $i$	73.0 deg
Radius of maximum warp $R_{mw}$	$1.7 \times r_{NS}$
Warp opening angle $\theta_w$	$40.8 \pm 1.5 \text{ deg}$
Disk angular semi-thickness $\theta_d$	8.0 deg
Tilt of inner disk to orbital plane $\alpha_d$	$4.1 \pm 0.4 \text{ deg}$
Line-of-nodes parameter $\Delta\psi$	$2.95 \pm 0.04$

<sup>1</sup> $1\sigma$  errors are given for fitted parameters. Parameters without errors are as taken from Cowley, Crampton, & Hutchings 1979, McClintock *et al.* 1984, and Paper I.

TABLE 2. ASCA (GIS3) SPECTRAL FITS (0.6 - 10 keV)<sup>1</sup>

Parameter	A1-4 <sup>2</sup>	A6-8 <sup>2</sup>	A9-11 <sup>2</sup>	PV Phase <sup>3</sup>
Exposure time (s)	6,592	6,010	6,272	22,703
Count rate (cts s <sup>-1</sup> )	84.6±0.1	81.4±0.1	85.8±0.1	84.9±0.1
N <sub>H</sub> <sup>4</sup> (10 <sup>21</sup> cm <sup>2</sup> )	0.7±0.5	0.1±0.4	0.5±0.1	1.8±0.2
CompST <sup>5</sup> kT (keV)	2.1±0.1	2.1±0.1	2.0±0.1	1.6±0.02
CompST $\tau$	25±4	29±5	27±6	23±1
Blackbody <sup>6</sup> kT (keV)	0.54±0.01	0.55±0.02	0.60±0.01	0.62±0.02
Fraction of energy flux from blackbody	0.16	0.20	0.10	0.10
Line <sup>7</sup> energy (keV)	1.02±0.2	1.09±0.4	0.95±0.3	1.02±0.3
Line width (keV)	0.2±0.2	0.3±0.2	0.2±0.2	0.11±0.02
Eq. width of line (eV)	66	75	94	38
Reduced $\chi^2$	1.4	1.2	1.4	1.8

<sup>1</sup>All errors given are 1  $\sigma$ .

<sup>2</sup>ASCA observation identifier: 43029000.

<sup>3</sup>ASCA observation identifier: 40017000.

<sup>4</sup>N<sub>H</sub> is the neutral hydrogen column density. The effective absorption cross section  $\sigma(E)$  was calculated on the assumption of neutral cosmic-abundance material (Morrison and McCammon 1983).

<sup>5</sup>Comptonization model of Sunyaev & Titarchuk (1980; Comptonization of cool photons on hot electrons).

<sup>6</sup>N(E)(cm<sup>-2</sup> s<sup>-1</sup> keV<sup>-1</sup>) = A<sub>BB</sub>(e<sup>E/kT</sup>-1)E<sup>2</sup>

<sup>7</sup>A simple Gaussian.

N(E)(cm<sup>-2</sup> s<sup>-1</sup> keV<sup>-1</sup>) = A<sub>Line</sub>(1/( $\sqrt{2\pi\sigma^2}$ ))e<sup>(-0.5(E-E<sub>Line</sub>)<sup>2</sup>/σ<sup>2</sup>)</sup>

E is energy in keV; T is temperature in Kelvin,  $k$  is the Boltzmann constant, A<sub>BB</sub> and A<sub>Line</sub> are normalization constants.

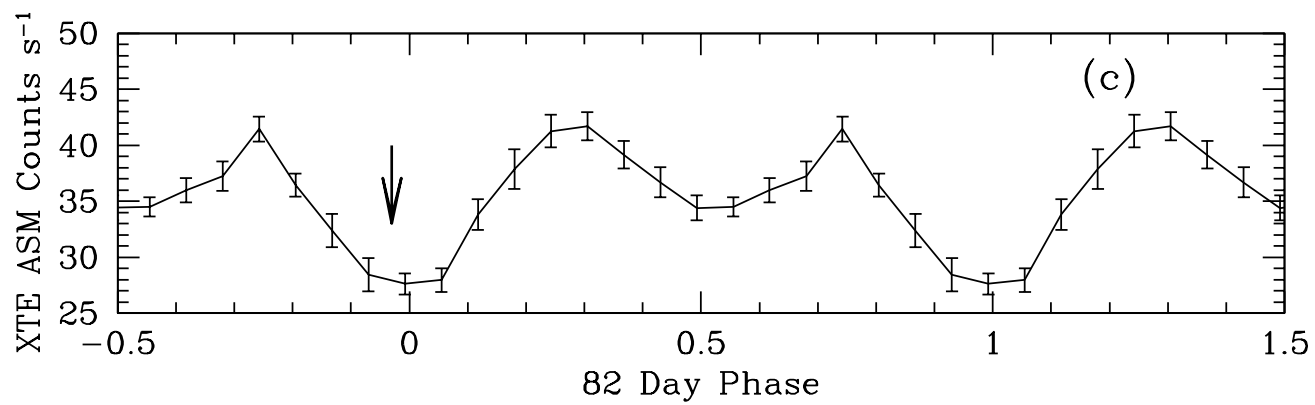
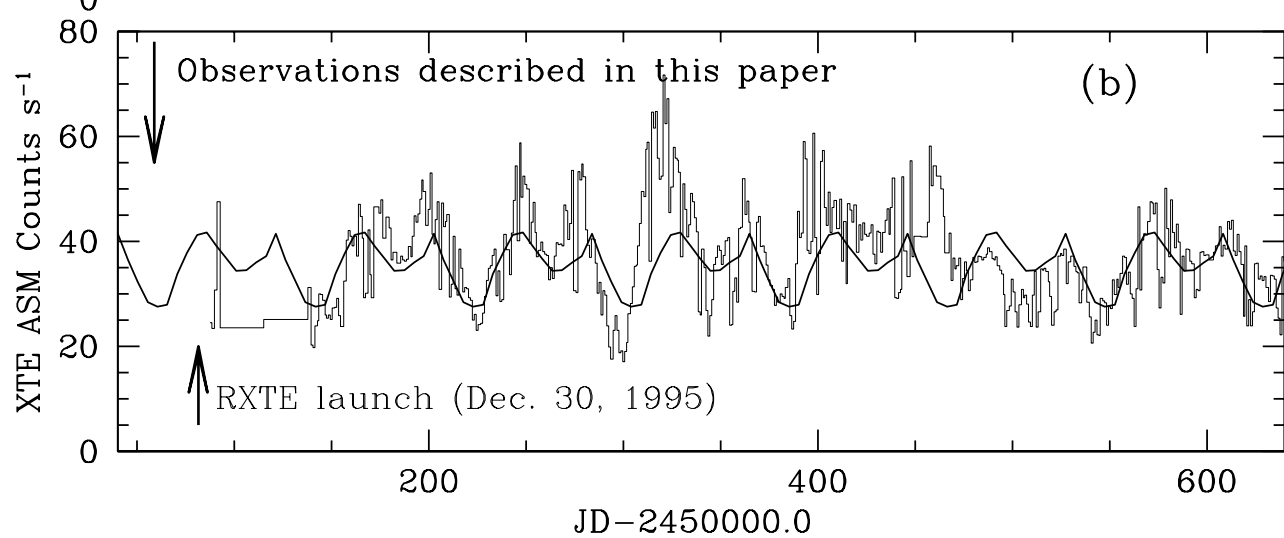
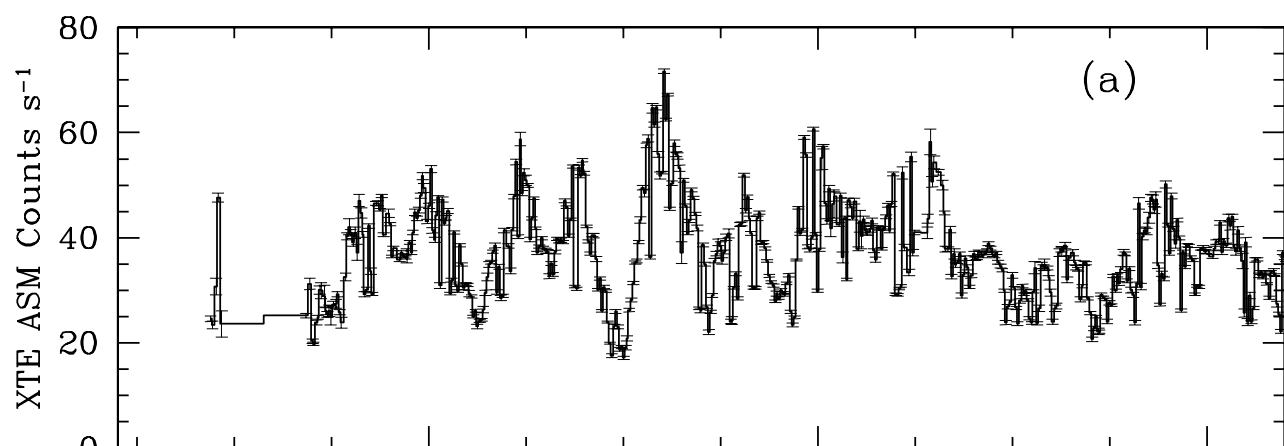
TABLE 3. ULTRAVIOLET LINE FLUXES AND VELOCITIES

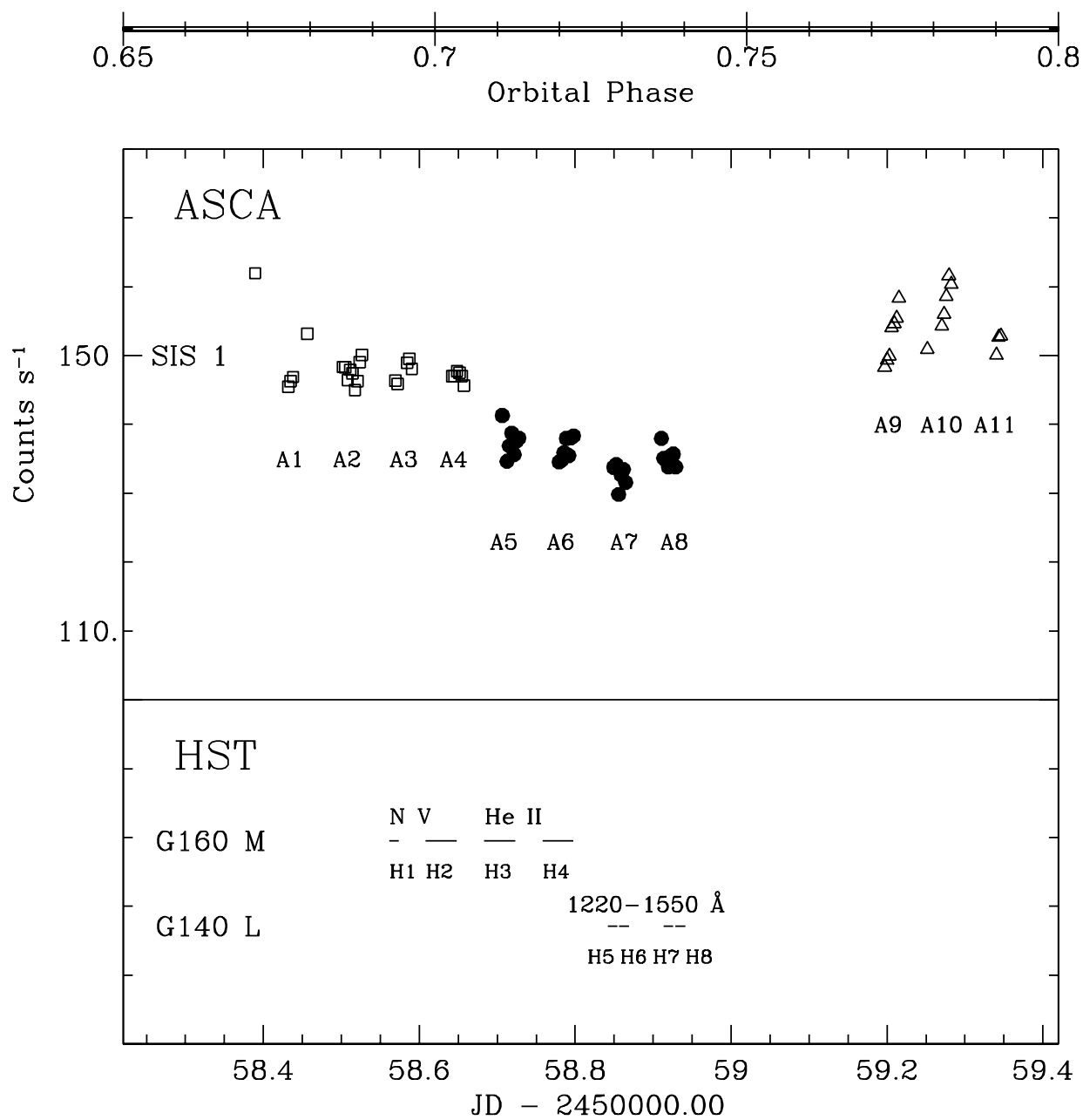
HST OBS No.	Feature	Flux (erg s <sup>-1</sup> cm <sup>-2</sup> )	FWHM (km s <sup>-1</sup> )	Velocity <sup>1</sup> (km s <sup>-1</sup> )
H1 <sup>2</sup> G160M	N V 1238 N V 1242	5.9±0.8(-14) 3.8±0.7(-14)	272±25 239±31	-99±10 -92±13
H2 G160M	N V 1238 N V 1242	4.8±0.4(-14) 3.9±0.4(-14)	336±23 316±24	-94±9 -93±9
H3 G160M	He II 1640	3.1±0.6(-14)	343±46	-145±20
H4 G160M	He II 1640	2.8±0.6(-14)	327±46	-140±29
H5 G140L	1290-1550Å Si IV 1394 Si IV 1403 N IV] 1486 C IV 1548	8.87(-13) 1.3±0.2(-14) 0.9±0.2(-14) 1.1±0.2(-14) >7.8(-15)	... 580±63 366±49 412±55 ...	... -162±26 -70±22 -179±25 -80 (at peak)
H6 G140L	1290-1550Å Si IV 1394 Si IV 1403 N IV] 1486 C IV 1548	8.89(-13) 1.2±0.2(-14) 0.9±0.2(-14) 1.3±0.2(-14) >5.5(-15)	... 591±69 426±57 492±66 ...	... -178±29 -150±25 -128±28 -140 (at peak)
H7 G140L	1290-1550Å Si IV 1394 Si IV 1403 N IV] 1486 C IV 1548	9.36(-13) 1.4±0.2(-14) 1.2±0.2(-14) 1.2±0.2(-14) >7.8(-15)	... 586±61 567±67 392±53 ...	... -175±26 -150±29 -162±23 -140 (at peak)
H8 G140L	1290-1550Å Si IV 1394 Si IV 1403 N IV] 1486 C IV 1548	8.66(-13) 1.4±0.2(-14) 1.3±0.2(-14) 1.0±0.2(-14) >1.0(-14)	... 642±63 476±47 296±34 ...	... -182±29 -148±21 -148±15 -100 (at peak)

<sup>1</sup>Heliocentric. Heliocentric velocity of center-of-mass of the Cyg X-2 system is  $-220 \text{ km s}^{-1}$  as given by Crampton, Cowley, & Hutchings (1979).

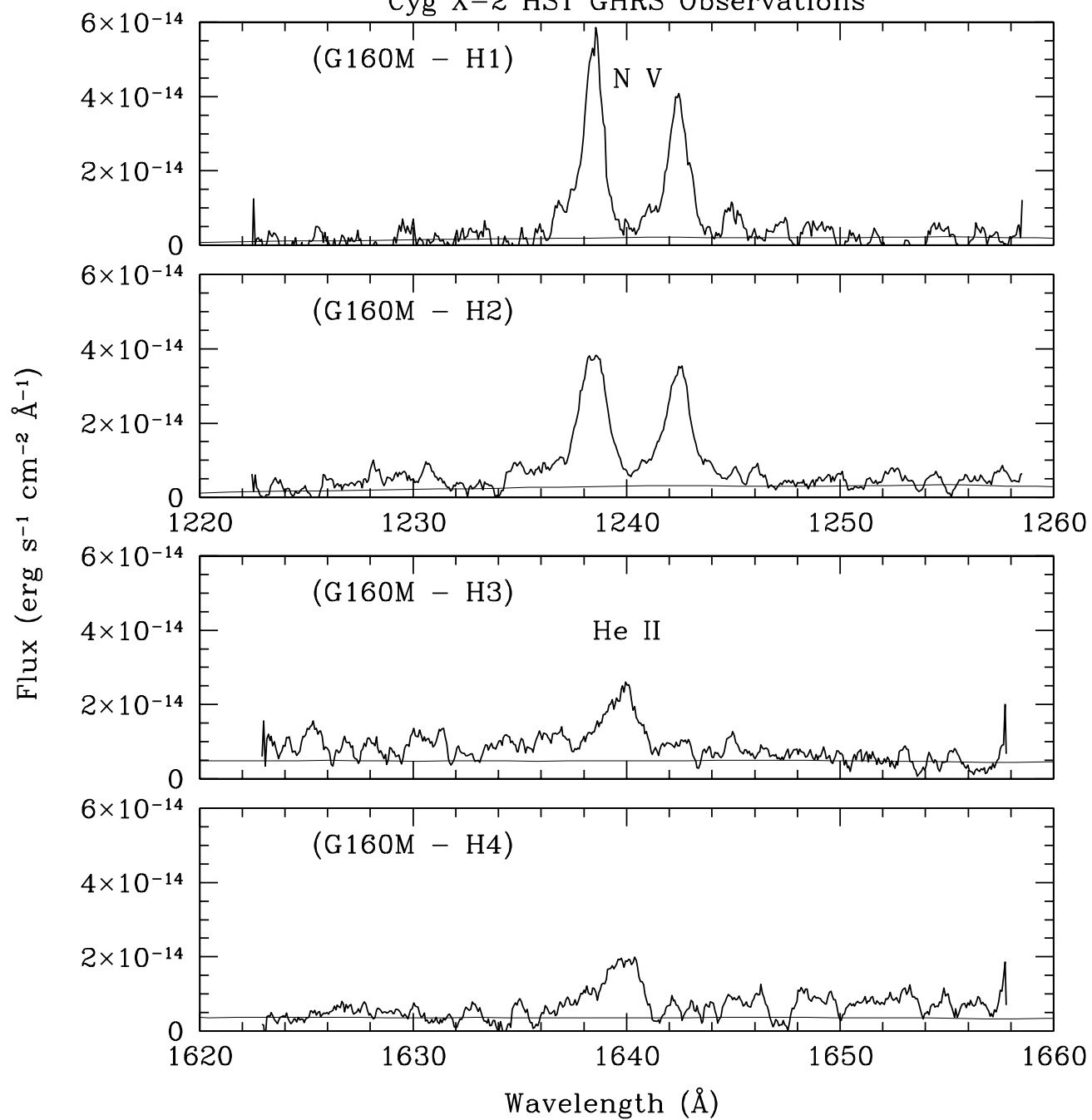
<sup>2</sup>The “H” numbers are the same as in Figure 2. The HST observation identifications are: Z31U01#T where # is 4 for H1; 6 for H2; 8 for H3 and Z3U010#T where # is A for H4; C for H5; E for H6; G for H7; and I for H8. Alternating number observations are SPYBAL exposures used for calibration. The line velocities have been corrected for the SPYBAL exposures.



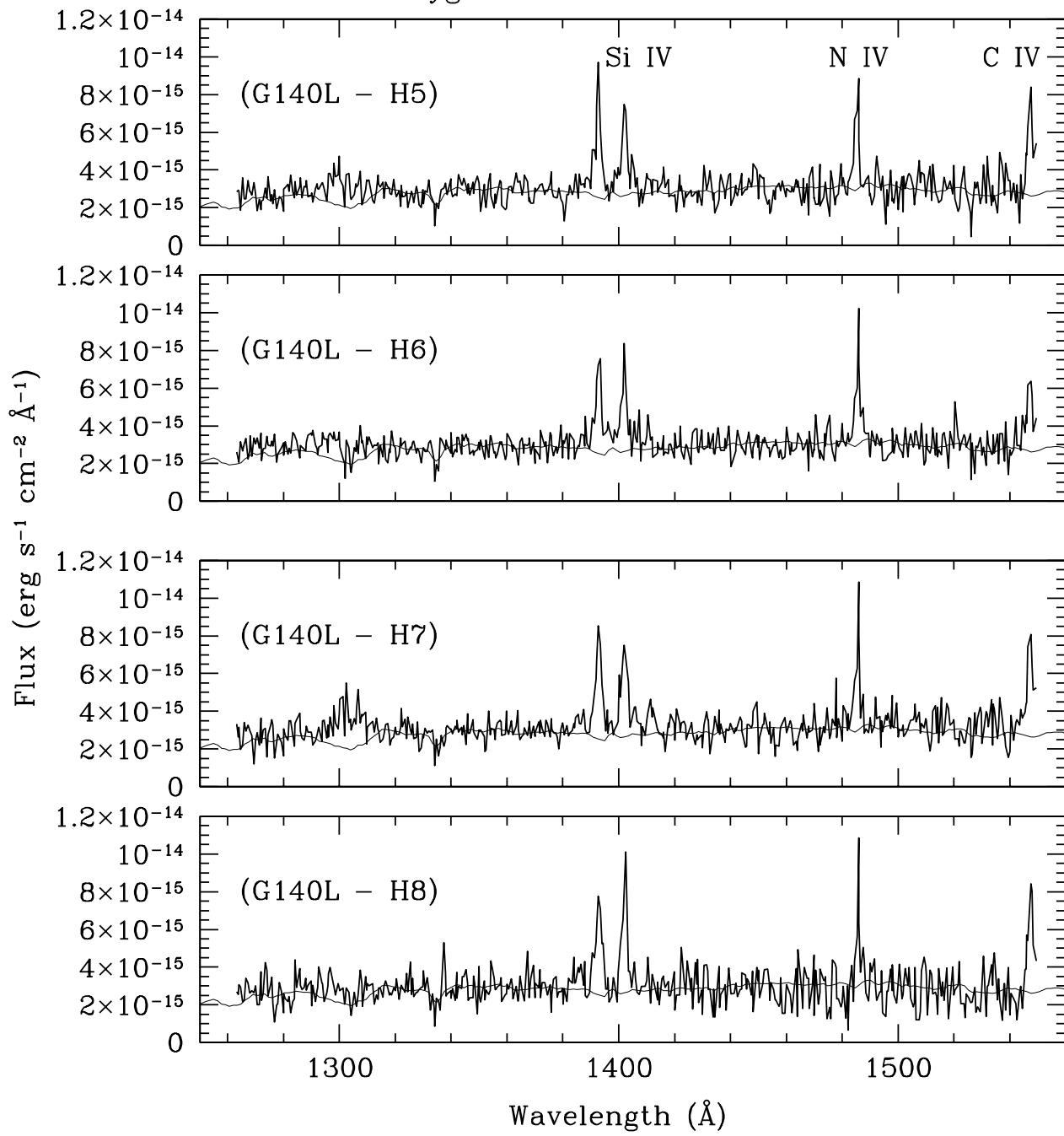


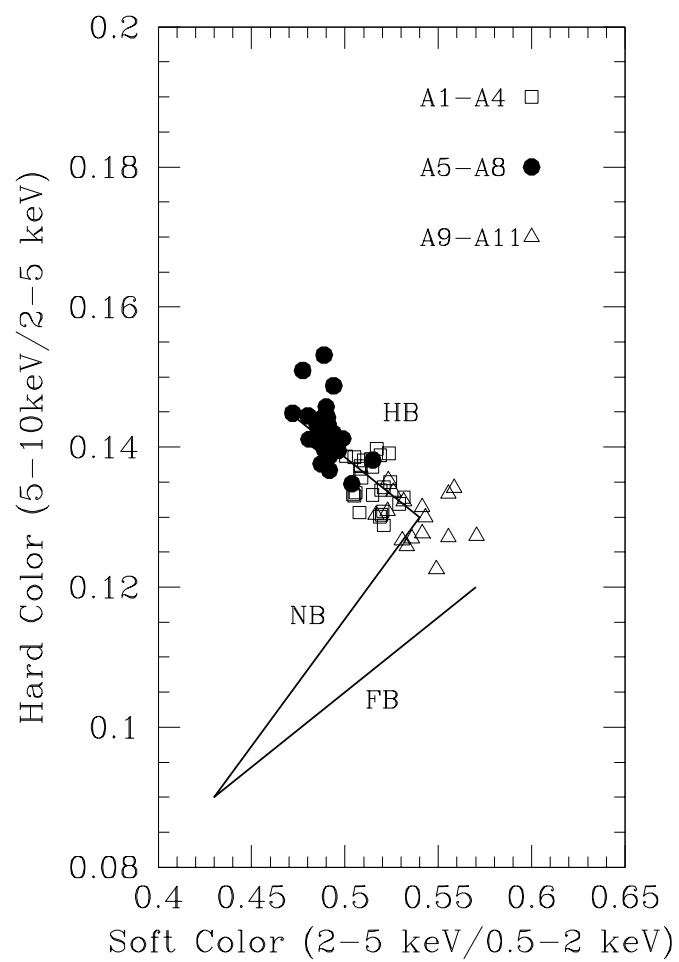


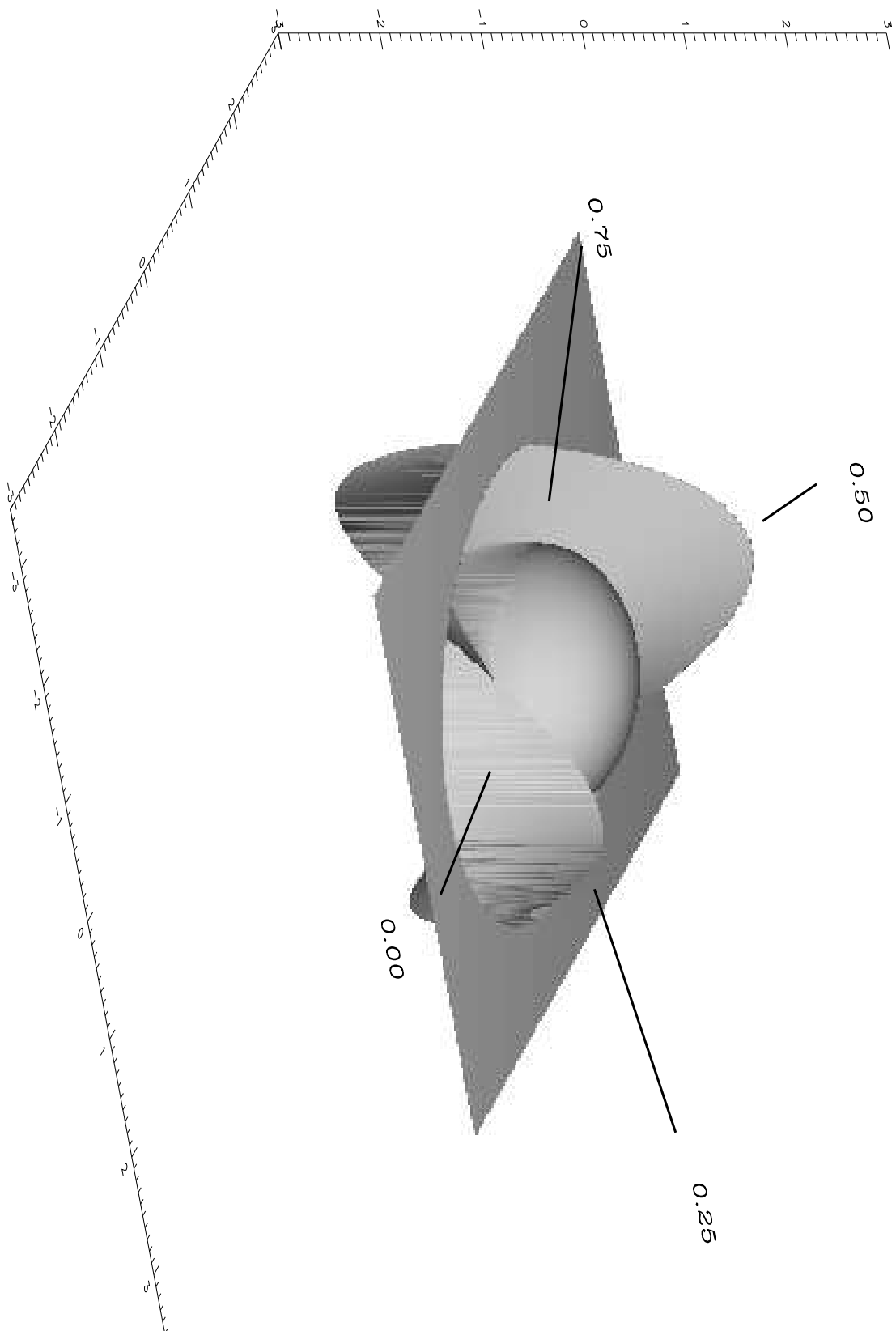
Cyg X-2 HST GHRS Observations

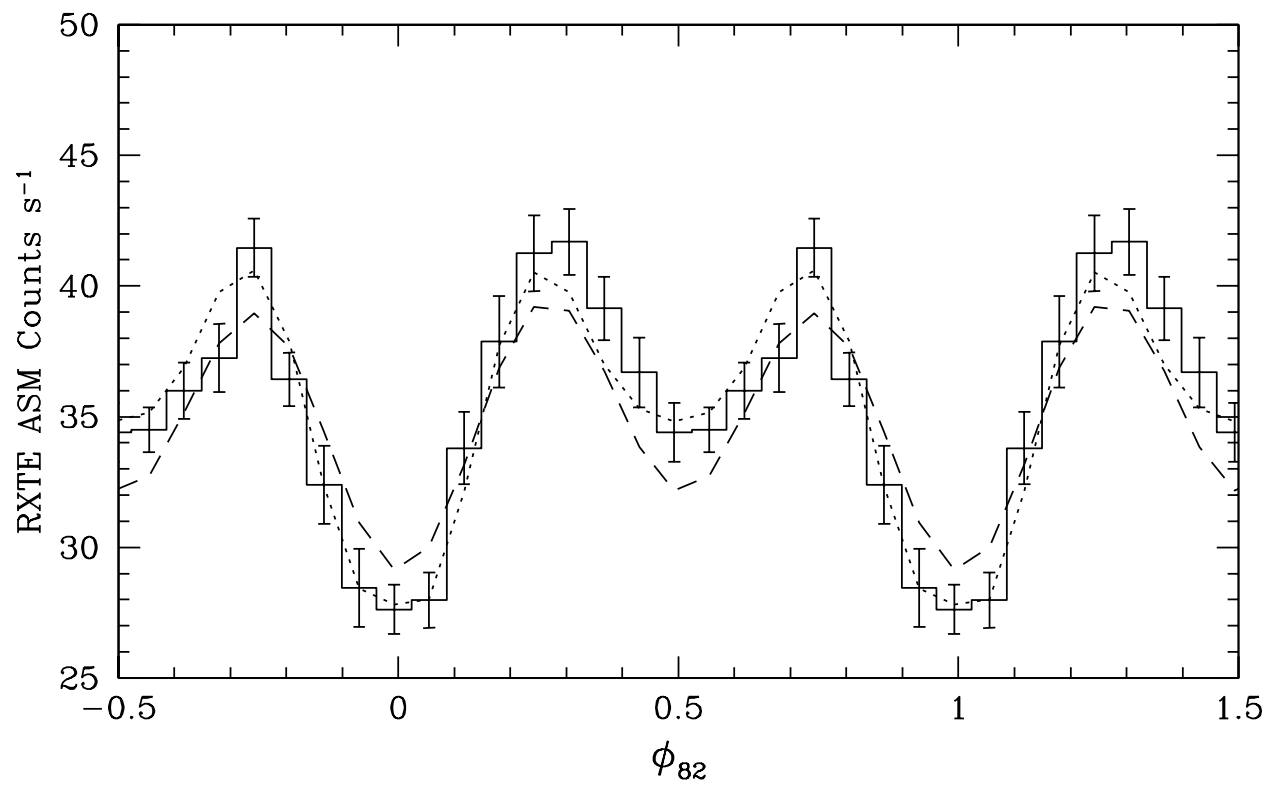


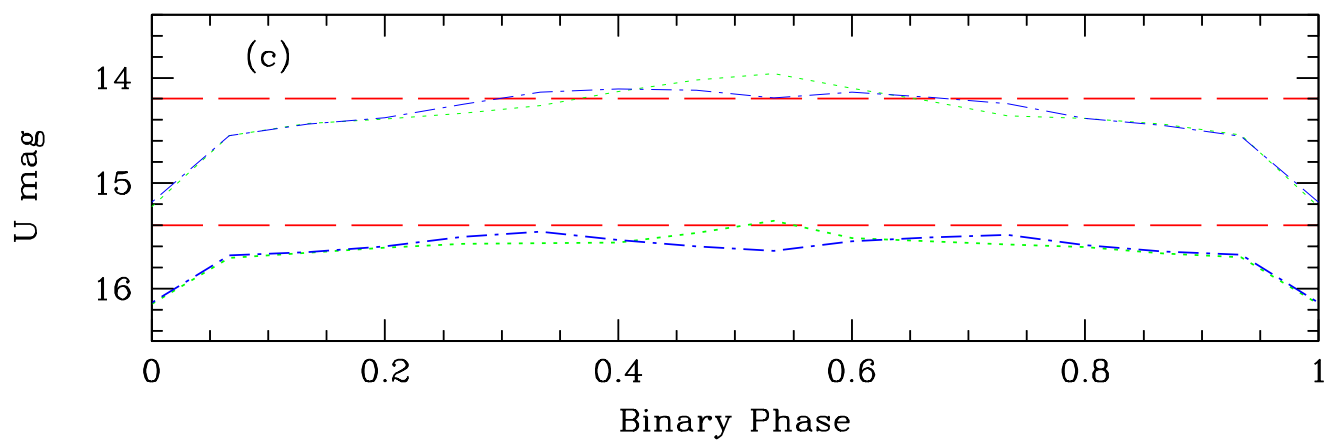
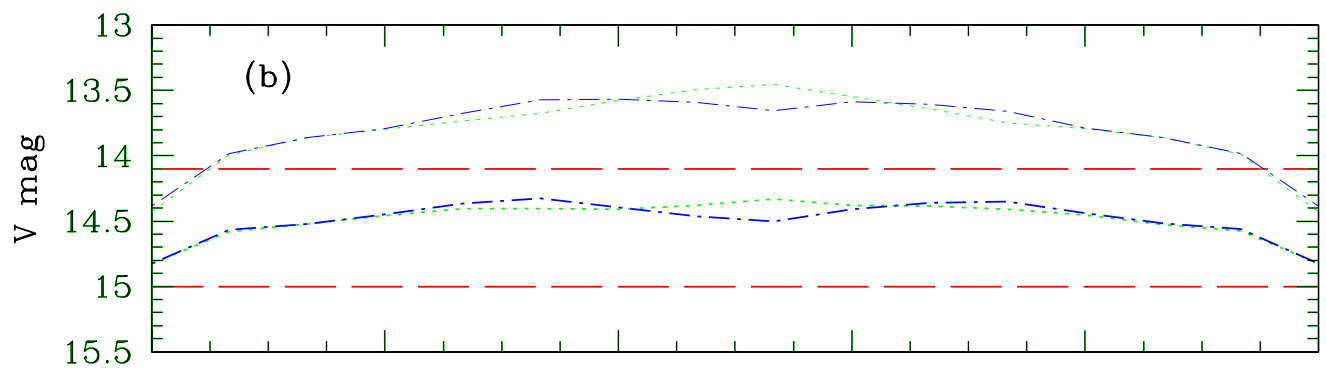
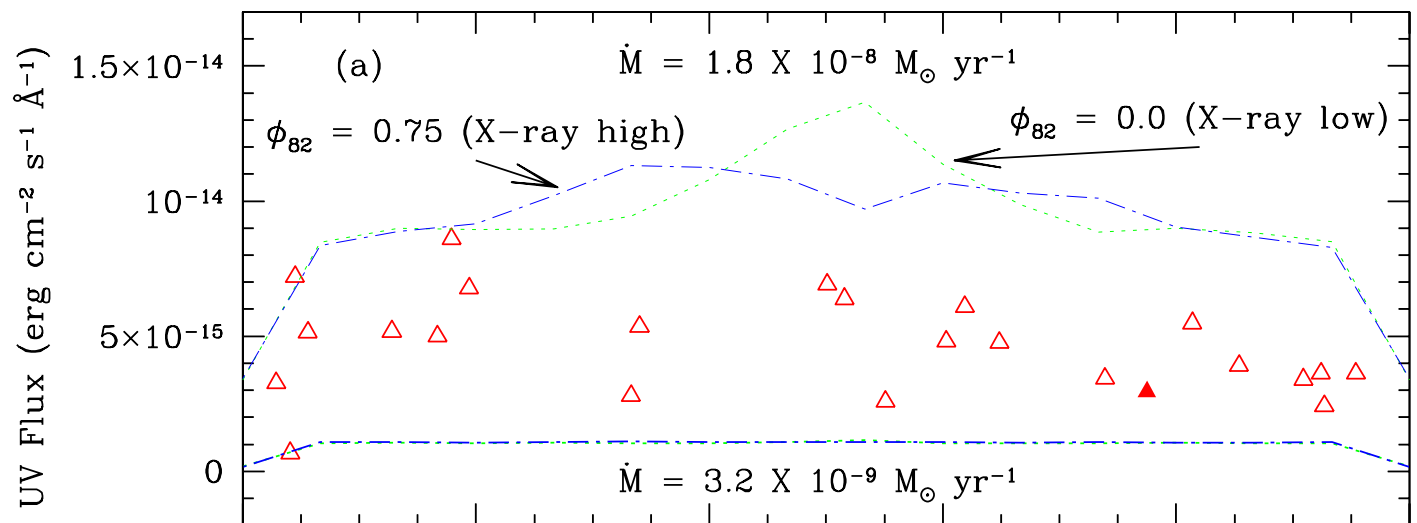
# Cyg X-2 GHRS Observations



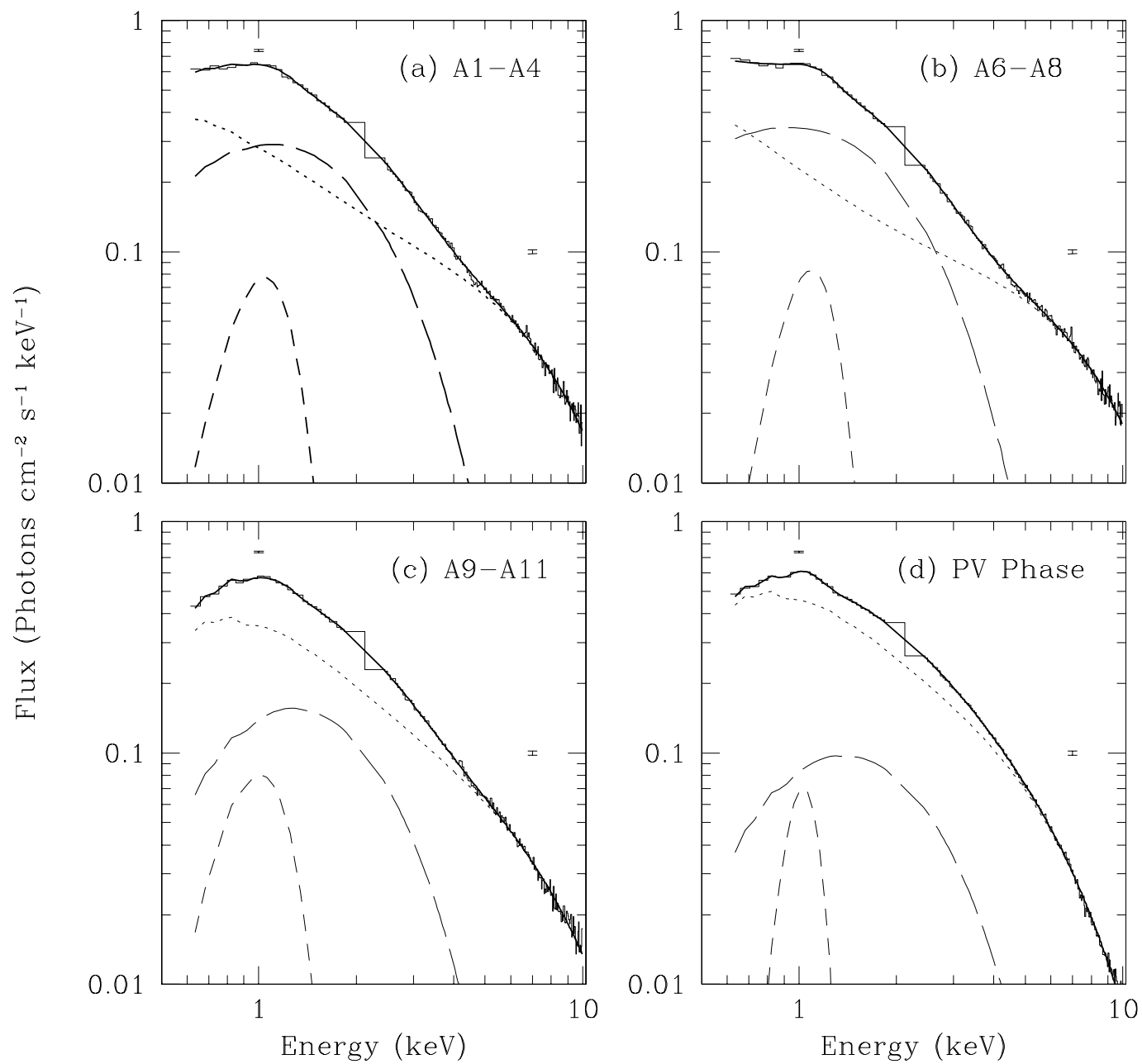












Cyg X-2 NV Line Profile (H2)

